A mean-field homogenisation scheme with CZM-based interfaces describing progressive inclusions debonding

Timothée Gentieu[a,c], Anita Catapano[b,*], Julien Jumel[a], James Broughton[c]

[a] *Université de Bordeaux, I2M CNRS UMR 5295, F-33400 Talence, France*
[b] *Bordeaux INP, Université de Bordeaux, I2M CNRS UMR 5295, F-33400 Talence, France*
[c] *Oxford Brookes University (OBU), Wheatley Campus, OX331HX, UK*

Abstract

The objective of the present study is to describe the progressive debonding of inclusions in particle or fibre reinforced composites. To do so, the mean-field homogenisation scheme of Mori-Tanaka is enriched to take into account imperfect interfaces. The interfaces are modelled by a bilinear Cohesive Zone Model (CZM) taking into account normal and tangential effects. Results obtained with this new mean-field homogenisation scheme are compared to 2D FE-based numerical simulations that are used as reference results. The effects of inclusions volume fraction and size are also observed.

Keywords: Particle-reinforced composites, Homogenisation, Cohesive zone models, Debonding, Finite element method

1. Introduction

Reinforced composites are commonly used in various industries such as automotive, aeronautics, or aerospace. The matrix can be reinforced with particles or fibres to satisfy numerous requirements in terms of mechanical properties. The resulting mechanical properties depend on the components properties, the size and shape of the inclusions, and the adhesion between the inclusions and the matrix [1–3]. For the purpose of the design process, simple laws describing the material behaviour are preferred because they can easily be implemented in large scale structures. Mean-field homogenisation techniques are then a good way to describe the material behaviour. In the

*Corresponding author. Tel.: +33 5 56 84 61 06
Email address: anita.catapano@bordeaux-inp.fr (Anita Catapano)

present study, only the Mori-Tanaka homogenisation scheme [4], [5] is considered but multiple schemes with different levels of sophistication have been developed in the literature (e.g. self-consistent scheme [6], [7], differential scheme [8], Lielens [9], etc.).

In order to develop more realistic analytical models some researchers attempted to take into account non-linear effects such as the debonding between the inclusions and the matrix [10] within the framework of homogenisation schemes. This type of model was notably developed for high explosive materials to predict the decohesion between energetic particles in a polymeric binder matrix. They first determined the mechanical properties of particles/matrix interfaces based on a bilinear Cohesive Zone Model (CZM) approach [11]. Then, the cohesive behaviour of interfaces was introduced into High-Dilute and Mori-Tanaka homogenisation schemes under hydrostatic loading conditions [12] and uniaxial loading [13]. Comparisons with numerical results showed good correlation between numerical and analytical models especially concerning the evaluation of particle volume fraction and size effects on particle debonding [14].

In the present work, a new mean-field homogenisation scheme is presented. This model is an improved version of the Mori-Tanaka model which is enriched to take into account imperfect interfaces through the introduction of a CZM. The main novelty of the present method concerns the integration of the evolution of the compliance of the interface through a convergence loop based on a CZM law. In order to prove the effectiveness of the proposed model, results are compared with those obtained from a FE-based analysis. This comparison let assess the effects of morphological parameters of the composite material (volume fraction and size of the inclusions) that gives valuable information on the behaviour of reinforced composites. The paper is organised as follows: Section 2 focuses on the description of imperfect interfaces in the framework of mean-field homogenisation schemes, Section 3 presents the Mori-Tanaka model with weakened interfaces, Section 4 introduces the theory of CZMs whilst Section 5 describes the new Mori-Tanaka model combined with CZMs for describing the imperfect interfaces. Numerical results are presented in Section 6 and Section 7 ends the paper with some concluding remarks.

2. Analytical modelling of linear spring-type imperfect interfaces

In this study of the homogenisation of particle reinforced composites, an imperfect elastic bonding between the inclusions and the matrix is considered. Following the concept developed by Qu in [15] and [16], the imperfect

interfaces between two phases can be modelled by introducing an infinitely thin layer in which transferred stresses remain continuous and displacements become discontinuous (see Fig. 1). S is used to denote the surface of the interface and $\vec{n}$ its outward normal vector. S^+ represents the interface when approaching it from outside the inclusion and S^- when approaching it from inside the inclusion. The stress at the interface being continuous, normal stress jump $\Delta\sigma$ between the phases is null:

$$\Delta\sigma_{ij}n_j = \left[\sigma_{ij}\left(S^+\right) - \sigma_{ij}\left(S^-\right)\right] n_j = 0 \tag{1}$$

The displacement jump Δu is here modelled with a linear spring:

$$\Delta u_i = \left[u_i\left(S^+\right) - u_i\left(S^-\right)\right] = \eta_{ij}\sigma_{jk}n_k \tag{2}$$

The second order tensor η_{ij} represents the compliance of the spring/layer interface. It is assumed to be symmetric and definite positive. One can recognise a perfect interface when η_{ij} is set to zero whereas $\eta_{ij} \to \infty$ implies a complete debond. Two parameters α and β are introduced to model the interface compliance respectively in the tangential and normal direction of the interface (see Fig. 1). The interface compliance tensor is given by the relationship:

$$\eta_{ij} = \alpha\delta_{ij} + (\beta - \alpha)\, n_i n_j \tag{3}$$

where α and β represent the tangential and normal compliances of the interface, and δ the Kronecker symbol. Therefore, the tangential and normal displacement jump can be expressed as follows:

$$\Delta u_i\left(\delta_{ik} - n_i n_k\right) = \alpha\sigma_{ij}n_j\left(\delta_{ik} - n_i n_k\right) \tag{4}$$

$$\Delta u_i n_i = \beta\sigma_{ij}n_j n_i \tag{5}$$

Considering Eqs. 4-5, a new relationship between the perturbation strain field $\underset{\sim}{\boldsymbol{\epsilon}}^d$ in the inclusion and the eigenstrain $\underset{\sim}{\boldsymbol{\epsilon}}^*$ can be established:

$$\epsilon^d_{ij}(\underline{x}) = S^{Esh}_{ijkl}\epsilon^*_{kl} - C_{klmn}\int_S \Delta u_k(\underline{\xi})G_{ijmn}(\underline{\xi} - \underline{x})n_l\,\mathrm{d}S(\underline{\xi}), \tag{6}$$

where $\underset{\approx}{\boldsymbol{G}}$ is the Green function, $\underset{\approx}{\boldsymbol{S}}^{\boldsymbol{Esh}}$ is the inclusion Eshelby tensor, and $\underset{\approx}{\boldsymbol{C}}$ is the stiffness tensor of the matrix.

It is possible to determine a fourth-order tensor that relates the pertur-

bation strain to the eigenstrain: the modified Eshelby tensor $\underset{\approx}{\boldsymbol{S}}^{\boldsymbol{EshM}}$. With the introduction of a compliant interface, the eigenstrain is not homogeneous in the inclusion any more. To overcome this difficulty, [16] calculated a volume averaged modified Eshelby tensor by integrating the modified Eshelby tensor over the inclusion volume. [16] determined an exact solution of the problem by permutating the derivation and first integral operations of Eq. 6 and then permuting the surface and volume integrals of the same equation. However, Othmani et al [17] noticed that this is not a mathematically correct operation as, according to Fubini's theorem, such permutations are only allowed when the integration volume is free from any singularity (which is not the case here as Green's function is singular along the imperfect interface).

To perform the calculation of the volume averaged modified Eshelby tensor, [17] got rid of Green's function singularity by translating the calculations in Fourier space. Othmani obtained the following expression of the modified Eshelby tensor (for convenience, here below the volume averaged will be omitted):

$$\underset{\approx}{\boldsymbol{S}}^{\boldsymbol{EshM}} = \left[\underset{\approx}{\boldsymbol{I}} + \langle\underset{\approx}{\boldsymbol{\Gamma}}\rangle_{\Omega}\right]^{-1} : \left[\underset{\approx}{\boldsymbol{S}}^{\boldsymbol{Esh}} + \langle\underset{\approx}{\boldsymbol{\Gamma}}\rangle_{\Omega}\right], \tag{7}$$

while Qu has the following one:

$$\underset{\approx}{\boldsymbol{S}}^{\boldsymbol{EshM}} = \underset{\approx}{\boldsymbol{S}}^{\boldsymbol{Esh}} + \langle\underset{\approx}{\boldsymbol{\Gamma}}\rangle_{\Omega} : \left(\underset{\approx}{\boldsymbol{I}} - \underset{\approx}{\boldsymbol{S}}^{\boldsymbol{Esh}}\right). \tag{8}$$

For both Eqs. 7-8, the tensor $\langle\underset{\approx}{\boldsymbol{\Gamma}}\rangle_{\Omega}$ is expressed as:

$$\langle\underset{\approx}{\boldsymbol{\Gamma}}\rangle_{\Omega} = \left(\underset{\approx}{\boldsymbol{I}} - \underset{\approx}{\boldsymbol{S}}^{\boldsymbol{Esh}}\right) : \underset{\approx}{\boldsymbol{H}} : \underset{\approx}{\boldsymbol{C}}_{\boldsymbol{m}}, \tag{9}$$

$$\text{with } H_{ijkl} = \frac{1}{\Omega}\int_S (\eta_{ik}n_jn_l + \eta_{jk}n_in_l + \eta_{il}n_jn_k + \eta_{jl}n_in_k)\,\mathrm{d}S, \tag{10}$$

where $\underset{\approx}{\boldsymbol{H}}$ is a fourth-order tensor representing the influence of both the interface compliance and the morphology of the inclusion. Analytical expressions of this tensor are given by Qu for specific cases where the shape of the inclusions enables the calculation of the integrals analytically. Othmani [17] claimed that the derivation of this tensor was also wrong in [16], however a comparison of the expressions given by both in the case of a spherical

particle reveals the same result. $\underset{\approx}{\boldsymbol{H}}$ can always be decomposed as follows:

$$\underset{\approx}{\boldsymbol{H}} = \alpha \underset{\approx}{\boldsymbol{P}} + (\beta - \alpha) \underset{\approx}{\boldsymbol{Q}}. \tag{11}$$

For specific inclusion geometries, the expressions of $\underset{\approx}{\boldsymbol{P}}$ and $\underset{\approx}{\boldsymbol{Q}}$ can be analytically determined. For a spherical particle of radius a, one gets:

$$P_{ijkl} = \frac{1}{a} I_{ijkl} \tag{12}$$

$$Q_{ijkl} = \frac{1}{5a} \left(2I_{ijkl} + \delta_{ij}\delta_{kl}\right) \tag{13}$$

For the case of a cylindrical inclusion of radius a, (based on [18]) one can obtain the following expressions:

$$P_{1111} = P_{2222} = 4P_{2323} = 4P_{1313} = 2P_{1212} = \frac{1}{a}, \tag{14}$$

$$Q_{1111} = Q_{2222} = 3Q_{1122} = 3Q_{2211} = 3Q_{1212} = \frac{3}{4a}, \tag{15}$$

$$P_{ijkl} = Q_{ijkl} = 0, \text{with } i,j,k,l = 1,2,3. \tag{16}$$

The strain localisation tensors obtained by Qu and Othmani are also different. Othmani obtained (and was confirmed by [18]):

$$\underset{\approx}{\boldsymbol{A}}_{\boldsymbol{i}}^{\boldsymbol{HD}} = \left[\underset{\approx}{\boldsymbol{I}} - \underset{\approx}{\boldsymbol{S}}^{\boldsymbol{EshM}} : \left(\underset{\approx}{\boldsymbol{I}} - \underset{\approx}{\boldsymbol{C}}_{\boldsymbol{m}}{}^{-\mathbf{1}} : \underset{\approx}{\boldsymbol{C}}_{\boldsymbol{i}}\right)\right]^{-1} : \left[\underset{\approx}{\boldsymbol{I}} + \left\langle \underset{\approx}{\boldsymbol{\Gamma}} \right\rangle_{\Omega}\right]^{-1}, \tag{17}$$

while Qu reported:

$$\underset{\approx}{\boldsymbol{A}}_{\boldsymbol{i}}^{\boldsymbol{HD}} = \left[\underset{\approx}{\boldsymbol{I}} - \underset{\approx}{\boldsymbol{S}}^{\boldsymbol{EshM}} : \left(\underset{\approx}{\boldsymbol{I}} - \underset{\approx}{\boldsymbol{C}}_{\boldsymbol{m}}{}^{-\mathbf{1}} : \underset{\approx}{\boldsymbol{C}}_{\boldsymbol{i}}\right)\right]^{-1}. \tag{18}$$

In the present work, to check the correction applied to the modified Eshelby tensor and the strain localisation tensor, the strain in an inclusion subjected to a remote hydrostatic loading is numerically determined and compared to the analytical prediction from Qu [16] and from the corrected expressions [17] and [18]. A compliant interface is introduced between the inclusion and the matrix ($\alpha = \beta = 4 \times 10^{-5}$ mm/MPa). Two types of inclusions are used: a spherical particle of radius $a = 100$ μm and a cylinder of radius $a = 100$ μm. The size of the unit cell is $L = 20 \times a$ so that boundary effects can be neglected. The calculations are made under axisymmetric and plane strain assumptions respectively for spherical and cylinder inclusion.

Fig. 2 represents the strain in the inclusion (homogeneous because of the hydrostatic applied loading) against the global strain of the material. In both cases, the corrected expressions almost give a perfect match with the numerical simulations while the results obtained with the expressions of Qu diverge. This test validates the corrected expressions of the modified Eshelby tensor and the strain localisation tensor.

3. Mori-Tanaka model with weakened interfaces

Exploiting the theory presented in Section 2, a single inclusion is considered within an infinite matrix (so that the interactions between the inclusions are completely neglected). The typical relationship of the mean-field homogenisation scheme to get the effective stiffness tensor C_{eff}, of a composite material made of $m+1$ phases, is:

$$\underset{\approx}{\boldsymbol{C}}_{\boldsymbol{eff}} = \sum_{r=0}^{m} \phi_r \underset{\approx}{\boldsymbol{A}}_{\boldsymbol{r}} : \underset{\approx}{\boldsymbol{C}}_{\boldsymbol{r}}, \tag{19}$$

where A_r and C_r are, respectively, the fourth order tensors of strain localisation and stiffness. ϕ_r is the phase volume fraction while the phase r=0 corresponds to the matrix material.

Mori and Tanaka [4] tried to take into account the effect of the inclusions interactions. For multiphasic materials, the Mori-Tanaka scheme can be generalised as follows:

$$\underset{\approx}{\boldsymbol{A}}_{\boldsymbol{r}}^{\boldsymbol{MT}} = \underset{\approx}{\boldsymbol{A}}_{\boldsymbol{r}}^{\boldsymbol{HD}} : \left(\sum_{r=0}^{n} \phi_r \underset{\approx}{\boldsymbol{A}}_{\boldsymbol{r}}^{\boldsymbol{HD}} \right)^{-1} \tag{20}$$

$$\underset{\approx}{\boldsymbol{C}}_{\boldsymbol{eff}} = \sum_{r=0}^{n} \phi_r \underset{\approx}{\boldsymbol{A}}_{\boldsymbol{r}}^{\boldsymbol{MT}} : \underset{\approx}{\boldsymbol{C}}_{\boldsymbol{r}} \tag{21}$$

where Eq. 20 represents the strain localisation tensor of the inclusion belonging to the r^{th} phase and Eq. 21 represents the effective stiffness tensor of the composite.

The mean-field homogenisation was revisited by Benveniste [5]. According to [5], the effect of the interaction between the particles can be modelled by replacing the remote loading by the strain inside the matrix phase. The strain localisation tensor of an inclusion becomes:

$$\underset{\approx}{\boldsymbol{A}}_{\boldsymbol{i}}^{\boldsymbol{MT}} = \underset{\approx}{\boldsymbol{A}}_{\boldsymbol{i}}^{\boldsymbol{HD}} : \left((1-\phi) : \underset{\approx}{\boldsymbol{A}}_{\boldsymbol{m}}^{\boldsymbol{HD}} + \phi \underset{\approx}{\boldsymbol{A}}_{\boldsymbol{i}}^{\boldsymbol{HD}} \right)^{-1} \tag{22}$$

Benveniste [5] demonstrated that the symmetry of the stiffness tensor is no longer certified when:

- more than two phases are taken into account;
- non-aligned ellipsoidal inclusions are considered.

Moreover, the Mori-Tanaka scheme give good results for low to moderate volume fraction of inclusions because interactions between inclusions are not properly described. However, thanks to the explicit formulation, it can be easily and quickly implemented and adapted to the specific volume fraction of the composited to be analysed.

The mean-field homogenisation scheme can be further improved using the modified Eshelby tensor to obtain the macroscopic behaviour of a composite material containing inclusions with imperfect interfaces. Esteva and Spanos [19] determined the effective elastic properties of nanotube reinforced composites with slightly weakened interfaces using a modified Mori-Tanaka scheme described thereafter. Lee and Pyo [20] used this approach to describe the evolution of the macroscopic behaviour with spherical particles considering that the progressive debonding could be represented with a reduction of interface stiffness.

Qu re-derived the Mori-Tanaka formulae with imperfect interfaces [16]. According to this procedure, the imperfect interfaces contribute to the evaluation of the strain in two ways [16]. First, the imperfect interfaces affect $\underset{\sim}{\boldsymbol{\epsilon}}_i$, the average strain, by taking into account the inhomogeneous distribution of strains. This effect can be taken into account by the use of the modified Eshelby tensor. Secondly, the imperfect interfaces introduce a displacement jump that induces another component $\underset{\sim}{\boldsymbol{\epsilon}}_{\boldsymbol{inter}}$ corresponding to the third term of the decomposition of the global strain E:

$$\underset{\sim}{\boldsymbol{E}} = (1-\phi)\,\underset{\sim}{\boldsymbol{\epsilon}}_m + \phi\underset{\sim}{\boldsymbol{\epsilon}}_i + \phi\underset{\approx}{\boldsymbol{H}} : \underset{\approx}{\boldsymbol{C}}_{\boldsymbol{i}} : \underset{\sim}{\boldsymbol{\epsilon}}_i. \tag{23}$$

The Mori-Tanaka strain localisation tensor for the phase i then becomes:

$$\underset{\approx}{\boldsymbol{A}}_{\boldsymbol{i}}^{\boldsymbol{MT}} = \underset{\approx}{\boldsymbol{A}}_{\boldsymbol{i}}^{\boldsymbol{HD}} : \left((1-\phi)\,\underset{\approx}{\boldsymbol{A}}_{\boldsymbol{m}}^{\boldsymbol{HD}} + \phi\left(\underset{\approx}{\boldsymbol{I}} + \underset{\approx}{\boldsymbol{H}} : \underset{\approx}{\boldsymbol{C}}_{\boldsymbol{i}}\right) : \underset{\approx}{\boldsymbol{A}}_{\boldsymbol{i}}^{\boldsymbol{HD}}\right)^{-1} \tag{24}$$

Thanks to this strain localisation tensor of Eq. (24) and the typical mean-field homogenisation formula (19), an estimate of the effective stiffness tensor can be obtained for a reinforced material with imperfect interfaces:

$$\underset{\approx}{\boldsymbol{C}}_{\boldsymbol{eff}} = (1-\phi)\,\underset{\approx}{\boldsymbol{A}}_{\boldsymbol{m}}^{\boldsymbol{MT}} : \underset{\approx}{\boldsymbol{C}}_{\boldsymbol{m}} + \phi\underset{\approx}{\boldsymbol{A}}_{\boldsymbol{i}}^{\boldsymbol{MT}} : \underset{\approx}{\boldsymbol{C}}_{\boldsymbol{i}} \tag{25}$$

4. Nonlinear interfaces based on a Cohesive Zone Model

A CZM is a zero thickness interface separation law where the stress vector at the interface is related to the displacement jump across the interface. Multiple shapes of traction-separation law have been proposed in the literature and a bilinear law was used for this study (based on Alfano & Crisfield work [21] and implemented in the commercial software Ansys). The bilinear traction-separation law is represented on Fig. 3 and the corresponding behaviour is defined by the following equations:

$$\begin{cases} \text{stage I: } \sigma_{int} & = \Delta u \ k_\sigma \\ \text{stage II: } \sigma_{int} & = \left(1 + \frac{k_{\tilde{\sigma}}}{k_\sigma}\right) \sigma_{max} - k_{\tilde{\sigma}} \ \Delta u \\ \text{stage III: } \sigma_{int} & = 0, \end{cases} \tag{26}$$

where k_σ and $k_{\tilde{\sigma}}$ are respectively the slopes of stage I and II of the traction-separation law. Stage I of the curve shows a linear elastic behaviour until ultimate stress is reached. Then, the cohesive stress at the interface linearly decreases as the interface stiffness is irreversibly decreasing proportionally to damage intensity. This cohesive law is governed by three main parameters: interface stiffness k_σ, strength σ_c and toughness. The initial slope is generally chosen according to numerical criteria. Indeed, the interface stiffness influences the effective stiffness of the RVE. Then, sufficiently high values are chosen so that the global elastic properties of the composite remain stable. The interface strength controls the damage initiation before a linear softening of the stress occurs until the stress completely vanishes and the interface is considered to be completely debonded. The whole elastic loading and damage process is governed by the interface fracture energy G_c which corresponds to the shaded area under the traction-separation curves.

For this study, only one set of parameter is employed, and is summarised in Table 1, where the elastic properties of the matrix and the inclusions are also gathered. The stiffness of the interface is set very high (equal to 2.5 10^6 MPa/mm) so that the global compliance of the material is unaffected by that of the interfaces whatever the size of the inclusions.

5. Introduction of the CZM in the Mori-Tanaka homogenisation scheme

The CZM traction-separation law is used to govern the evolution of the compliance of the interfaces. At each iteration, a new tensor $\underset{\approx}{\boldsymbol{H}}$ is calculated.

For both the cylindrical and spherical geometries of inclusions, it relies on two parameters α and β. Those two parameters are always considered equal for this study. They are computed at every iteration as the compliance of the interface evolves as the inverse of the stiffness of the traction-separation law.

The flowchart summarising the algorithm developed for the proposed homogenisation model is represented in Fig. 4. During the first phase of the loading, one obtains an elastic calculation with compliant interfaces. Then, once the limit strength of the interface is reached, the interfaces are damaged and their compliance increases according to the evolution of the CZM. To numerically simulate this phase, a convergence loop is employed:

- a first value of the stress at the inclusion interface (σ_i) is calculated using the value of the interface compliance at the previous step;
- the associated displacement of the interface is determined and a new value of the inclusion stress based on the CZM ($\sigma_{i\ test}$) is computed, as well as the associated compliance of the interface (β_{test})
- β_{test} is selected as the new compliance of the interface and the convergence loop is repeated until a convergence of the interface compliance is reached ($|\beta - \beta_{test}| < res$).

During the third phase of the loading, the inclusions are considered to be completely debonded (no stress transfer to the inclusions) and the inclusions are replaced by voids with the same geometry.

The calculation of the modified Eshelby tensor is particularly adapted to hydrostatic loading. To use the model under uniaxial axial tension, some assumptions have to be made (according to the one made in [17]):

1. The eigenstrain in the inclusions is assumed to be uniform;
2. Only a hydrostatic debond of the inclusions is considered (the evolution of the interfacial damage is the same in every direction);
3. The modified Eshelby tensor is averaged over the whole inclusion.

This procedure is based on the work of [16] which integrates imperfect elastic interfaces in the Mori-Tanaka homogenisation scheme. However, in the present work, there are some fundamental differences and novelties which concerns:

- the integration of the correct version of the modified Eshelby tensor developed in [17] (which is not been taken into account in [16]). In[18] of the correct modified Eshelby tensor is considered only for 2D circular particles ;
- the stiffness of the interface is governed by a CZM ([17] makes use of the same approach but within the highly diluted inclusions homogenisation scheme);
- the convergence loop used to catch the evolution of the stiffness of the interface is explicitly described unlike [17] where the procedure is not clearly exposed and can generate misunderstandings.

6. Comparisons with numerical results - Effect of morphological parameters

In order to evaluate the effectiveness of the propose analytical homogenisation model, the results have been compared with those of a 2D FE-based one (under plane strain assumption). Random 2D RVE with circular inclusions are generated using the Dropping and Rolling algorithm developed in [22]. The numerical implementation and Periodic Boundary Conditions are described in [22]. The FE model presented in [22] is modified in the present work by introducing Cohesive elements at all the interfaces between the inclusions and the matrix to numerically simulate the debonding of the particles from the matrix. Comparisons with numerical results are made for two different loading cases (in-plane bi-axial loading and uniaxial tension) to assess the capability of the model to be representative of the debonding phenomenon in reinforced composites.

The strain tensor considered for the bi-axial loading is the following:

$$\underset{\sim}{\boldsymbol{E}}_{\text{bi-axial}} = \begin{pmatrix} E & 0 & 0 \\ 0 & E & 0 \\ 0 & 0 & 0 \end{pmatrix}, \tag{27}$$

while for the uniaxial loading, it is:

$$\underset{\sim}{\boldsymbol{E}}_{\text{uniaxial}} = \begin{pmatrix} E & 0 & 0 \\ 0 & 0 & 0 \\ 0 & 0 & 0 \end{pmatrix}, \tag{28}$$

6.1. In plane bi-axial loading

The first loading case is the bi-axial one where equal displacements along the two in-plane directions x and y are applied to the RVE. A RVE with a 30% volume fraction ϕ of circular inclusions is selected (Fig. 5). All the inclusions have the same size ($R = 80$ μm). The stress-strain curve along x-direction, obtained using the FE model is represented with dots in Fig. 6 (a). This curve represents the reference values to be met. This curve can be divided into three parts. The first one corresponds to the elastic regime and all the interfaces behaviour belongs to stage I of the traction-separation law, Eq. 26. Then, inclusions start to debond and a global softening of the material is observed. In the final part, all the inclusions are completely debonded (no stress is redistributed to the inclusions) and one obtains another linear behaviour.

The analytical homogenisation model, presented in Section 5, is then employed and the resulting stress-strain curve is also plotted in red in Fig. 6 (a). The same trends corresponding respectively to inclusions completely bonded, debonding, and completely debonded, are also observed when using this model. Moreover, a good fit of the numerical results is observed, especially during the first and last phase. While in the middle part of the curve, i.e. during the debonding phase, only the very beginning of the FE-based results are correctly fitted. Indeed, in this part of the curve, a small load drop is observed with the numerical results whereas this phenomenon is not captured by the analytical homogenisation model.

The stress-displacement values of the interface determined at each corresponding point of the homogenisation model are plotted in Fig. 6 (b). One can see that they are perfectly superimposed with the adopted traction-separation law (continuous black line), confirming the good convergence of the homogenisation model.

6.2. Uniaxial loading

The same RVE of Fig. 5 is employed to test the homogenisation model under uniaxial loading along y-axis. The results from the semi-analytical and the numerical models are represented in Fig. 7 (a). Similar to the bi-axial, the behaviour of the material under uniaxial loading can be divided into three parts (inclusions completely bonded, debonding, and completely debonded) for both models. In the first part of the curve (elastic behaviour), the results for both models are almost superimposed. Then, as inclusions start to debond, the semi-analytical model seems to give a more compliant response than the numerical model. However, the starting point of the

debonding seems to be accurate. For the last phase (i.e. inclusion completely debonded), different slopes are observed for the semi-analytical and numerical models. They, nethertheless, roughly show the same qualitative behaviour. This can be explained by the fact that under uniaxial loading, when the inclusions are replaced by voids, these finally tend to collapse under the imposed loading. This behaviour is not representative of reality as the presence of the inclusion avoids this squashing effect. With the numerical model, inclusions are not completely debonded (at the equator) and a compressive stress is redistributed to the inclusions by Poisson's effect.

The stress-displacement point of the inclusion interfaces corresponding to the evolution of the loading are plotted in Fig. 7 (b). Once agin, similar to the bi-axial loading, a good match between the stress-strain homogenised curve given by the analytical model and the imposed traction-separation law is observed.

6.3. Parametric study: effect of inclusion volume fraction and size

In order to test the homogenisation model under multiple configurations, the effect of inclusion volume fraction is first evaluated and compared to numerical results. Concerning the FE models, RVEs with different inclusion volume fractions (20% to 60%) are generated using the same procedure as described in the previous subsections. All the inclusions are represented by circles of a 80 μm radius. The RVE obtained are depicted in Fig. 8.

The RVE are first loaded under bi-axial conditions. The obtained stress-strain curves are plotted in Fig. 9 (a). It is observed that the homogenised stiffness increases with inclusion volume fraction. In particular, the linear elastic parts of the curves are correctly estimated as there is very good agreement between the semi-analytical and numerical results. Both models then predict larger and more sudden load drops with increasing inclusion volume fraction. The semi-analytical and the numerical models especially show a good match to the results for low to moderate inclusion volume fractions (40% and below).

The same RVE ($\phi = 30\%$) but expanded in a homothetic manner is used to observe the effect of inclusion size. The results for both models are represented in Fig. 9 (b). The linear elastic part and the beginning of debonding region of the curve seem not be affected by the variation of the inclusion size (as the initial stiffness of the interface, the first slope of the CZM, was chosen very large compared the stiffnesses of the phases). However, the RVE with the largest particles show a more sudden load drop. The same observations were made in [14]. The last phase of the loading (completely debonded particles) is reached much faster when using large

particles compared with small ones. This strong particle size effect is also described in [23], which states that large particles tend to debond prior to smaller ones. The size effect is especially generated by the CZM in both the analytical and the numerical models as it introduces a length parameter in the problem. Indeed, the critical displacement u_c, characteristic of the CZM, is homogeneous to a length. It is also to be noted that the size of the inclusion intervenes in the calculation of the $\underset{\approx}{\boldsymbol{H}}$ tensor for the determination of the modified Eshelby tensor $\underset{\approx}{\boldsymbol{S}}^{\boldsymbol{EshM}}$.

The results for the inclusion volume fraction and size effects under uniaxial loading are represented in Fig. 10 (a) and (b) respectively. Similar to the bi-axial loading, good agreements are found between the semi-analytical and numerical results. Once again, the fit of the two models is the best at low to moderate inclusion volume fractions. Also under this loading condition, large particles debond prior to smaller ones.

7. Conclusion

A new semi-analytical homogenisation model based on a Mori-Tanaka homogenisation scheme, containing inclusions with imperfect interfaces, was developed through this study. To describe the progressive debonding of the reinforcements, the compliance of the inclusion interfaces evolves according to a bilinear traction-separation law, similar to that of a CZM.

The model is applicable to any type of inclusion geometry as long as its modified Eshelby tensor can be determined. This improved version of the homogenisation models presented in [16] and [17] led to better predictions of the influence of the imperfect interface behaviour on the resulting homogenised composite. Moreover, unlike the approaches of [16] and [17], this new model is able to simulate the debonding phase within an analytical homogenisation scheme. The results obtained with the present model were compared to that of numerical FE simulations based on 2D RVE under plane strain assumptions. The debonding was simulated using CZM. The same CZM parameters were attributed to both models so that no calibration of the semi-analytical model was required. Bi-axial and uniaxial loadings were tested. Given the debonding of the inclusions was considered to be hydrostatic, excellent agreements were found between the semi-analytical and numerical results under hydrostatic loading. Under bi-axial loading, the stress seemed to be slightly underestimated by the semi-analytical homogenisation model compared to that of the numerical one.

The effects of inclusion volume fraction and inclusion size were also tested. Similar trends were observed for both models:

- the volume fraction of particles stiffens the composite during the elastic loading but a higher load drop is observed as the particles start to debond. The effect of particle volume fraction on the debonding onset was not found to be a first order phenomenon;
- An important size effect is visible when debonding occured for large particles (large particles are debonded prior to smaller ones in accordance with the results of the literature [24] and [23]).

The proposed model could also be applied to a material containing inclusions of multiple sizes by considering the inclusions of different sizes as different phases. Accordingly, more slope changes would be observed when a greater number of inclusion populations are introduced. A continuous distribution of particles would then be required in order to obtain a smooth evolution of the homogenised stress-strain curves.

Acknowledgements

DGA of France, supporting the first author through *Allocation de thèse 2015*, is gratefully acknowledged.

Data availability statement

The data that support the findings of this study are available within the article and from the corresponding author, A. Catapano, upon reasonable request.

References

[1] L. Weng, T. Fan, M. Wen, Y. Shen, Three-dimensional multi-particle fe model and effects of interface damage, particle size and morphology on tensile behavior of particle reinforced composites, Composite Structures 209 (2019) 590–605 (2019). 1

[2] J. Dastgerdi, B. Anbarlooie, S. Marzban, G. Marquis, Mechanical and real microstructure behavior analysis of particulate-reinforced nanocomposite considering debonding damage based on cohesive finite element method, Composite Structures 122 (2015) 518–525 (2015).

[3] A. Shams, M. Porfiri, Analysis of particle–matrix interfacial debonding using the proper generalized decomposition, Composite Structures 111 (2014) 602–618 (2014). 1

[4] T. Mori, K. Tanaka, Average stress in matrix and average elastic energy of materials with misfitting inclusions, Acta Metal 21 (1973) 571 (1973). 2, 6

[5] Y. Benveniste, A new approach to the application of mori-tanaka's theory in composite materials, Mechanics of Materials 6 (1987) 147–157 (1987). 2, 6, 7

[6] R. Hill, A self-consistent mechanics of composite materials, Journal of the Mechanics and Physics of Solids 13 (4) (1965) 213–222 (1965). 2

[7] B. Budiansky, On the elastic moduli of some heterogeneous materials, Journal of the Mechanics and Physics of Solids 13 (4) (1965) 223–227 (1965). 2

[8] A. Norris, A differential scheme for the effective moduli of composites, Mechanics of materials 4 (1) (1985) 1–16 (1985). 2

[9] G. Lielens, P. Pirotte, A. Couniot, F. Dupret, R. Keunings, Prediction of thermo-mechanical properties for compression moulded composites, Composites Part A: Applied Science and Manufacturing 29 (1) (1998) 63–70 (1998). 2

[10] S. Ben, J. Zhao, Y. Zhang, Y. Qin, T. Rabczuk, The interface strength and debonding for composite structures: Review and recent developments, Composite Structures 129 (2015) 8–26 (2015). 2

[11] H. Tan, C. Liu, Y. Huang, P. Geubelle, The cohesive law for the particle/matrix interfaces in high explosives, Journal of the Mechanics and Physics of Solids 53 (8) (2005) 1892–1917 (2005). 2

[12] H. Tan, Y. Huang, C. Liu, P. Geubelle, The mori–tanaka method for composite materials with nonlinear interface debonding, International Journal of Plasticity 21 (10) (2005) 1890–1918 (2005). 2

[13] H. Tan, Y. Huang, C. Liu, G. Ravichandran, G. Paulino, Constitutive behaviors of composites with interface debonding: the extended mori–tanaka method for uniaxial tension, International Journal of Fracture 146 (3) (2007) 139–148 (2007). 2

[14] H. Inglis, P. Geubelle, K. Matouš, H. Tan, Y. Huang, Cohesive modeling of dewetting in particulate composites: micromechanics vs. multiscale finite element analysis, Mechanics of materials 39 (6) (2007) 580–595 (2007). 2, 12

[15] J. Qu, Eshelby tensor for an elastic inclusion with slightly weakened interface, Journal of applied mechanics 60 (4) (1993) 1048–1050 (1993). 2

[16] J. Qu, The effect of slightly weakened interfaces on the overall elastic properties of composite materials, Mechanics of Materials 14 (4) (1993) 269–281 (1993). 2, 4, 5, 7, 9, 10, 13

[17] Y. Othmani, L. Delannay, I. Doghri, Equivalent inclusion solution adapted to particle debonding with a non-linear cohesive law, International Journal of Solids and Structures 48 (24) (2011) 3326–3335 (2011). 4, 5, 9, 10, 13

[18] F. Dinzart, H. Sabar, New micromechanical modeling of the elastic behavior of composite materials with ellipsoidal reinforcements and imperfect interfaces, International Journal of Solids and Structures 108 (2017) 254–262 (2017). 5, 10

[19] M. Esteva, P. Spanos, Effective elastic properties of nanotube reinforced composites with slightly weakened interfaces, Journal of Mechanics of Materials and Structures 4 (5) (2009) 887–900 (2009). 7

[20] H. Lee, S. Pyo, Micromechanics-based elastic damage modeling of particulate compsites with weakened interfaces, Int. J. Solids Struct. 44 (2007) 8390–8406 (2007). 7

[21] G. Alfano, M. Crisfield, Finite element interface models for the delamination analysis of laminated composites: mechanical and computational issues, International journal for numerical methods in engineering 50 (7) (2001) 1701–1736 (2001). 8

[22] T. Gentieu, J. Jumel, A. Catapano, J. Broughton, Computational modelling of particulate-reinforced materials up to high volume fractions: Linear elastic homogenisation, Proceedings of the Institution of Mechanical Engineers, Part L: Journal of Materials: Design and Applications (2017) 1464420717707227 (2017). 10, 23

[23] T. Gentieu, J. Jumel, A. Catapano, J. Broughton, Size effect in particle debonding: Comparisons between finite fracture mechanics and cohesive zone model, Journal of Composite Materials (2018) 0021998318816471 (2018). 13, 14

[24] I. García, M. Paggi, V. Mantič, Fiber-size effects on the onset of fiber–matrix debonding under transverse tension: A comparison between cohesive zone and finite fracture mechanics models, Engineering Fracture Mechanics 115 (2014) 96–110 (2014). 14

Tables

	E $[GPa]$	ν [ ]	σ_{max} $[MPa]$	G_c $[J.m^{-2}]$
Particle	450	0.2	×	×
Matrix	3	0.3	×	×
Interface	×	×	50	100

Table 1: Mechanical properties of the materials

Figures

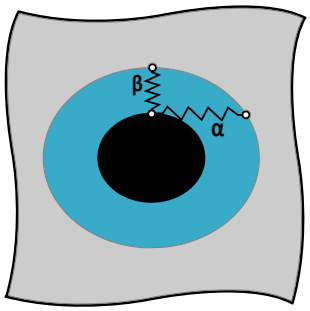

Figure 1: Imperfect interface modelled by a linear spring

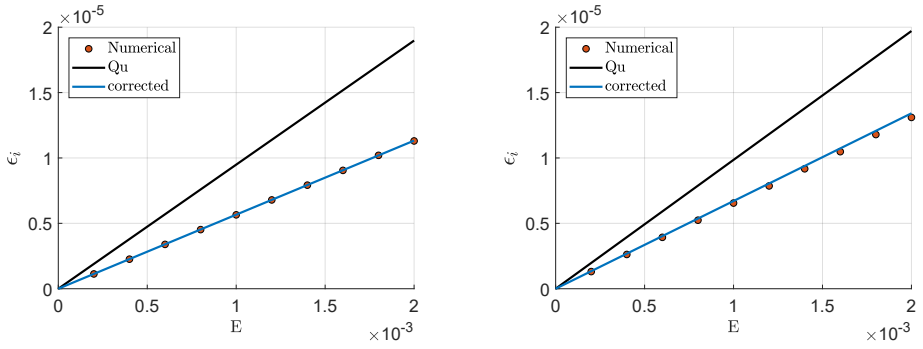

Figure 2: Strain concentration in the inclusion with (a) a spherical inclusion and (b) a cylindrical one.

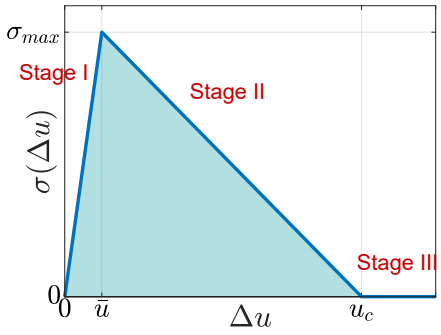

Figure 3: Bilinear traction-separation law.

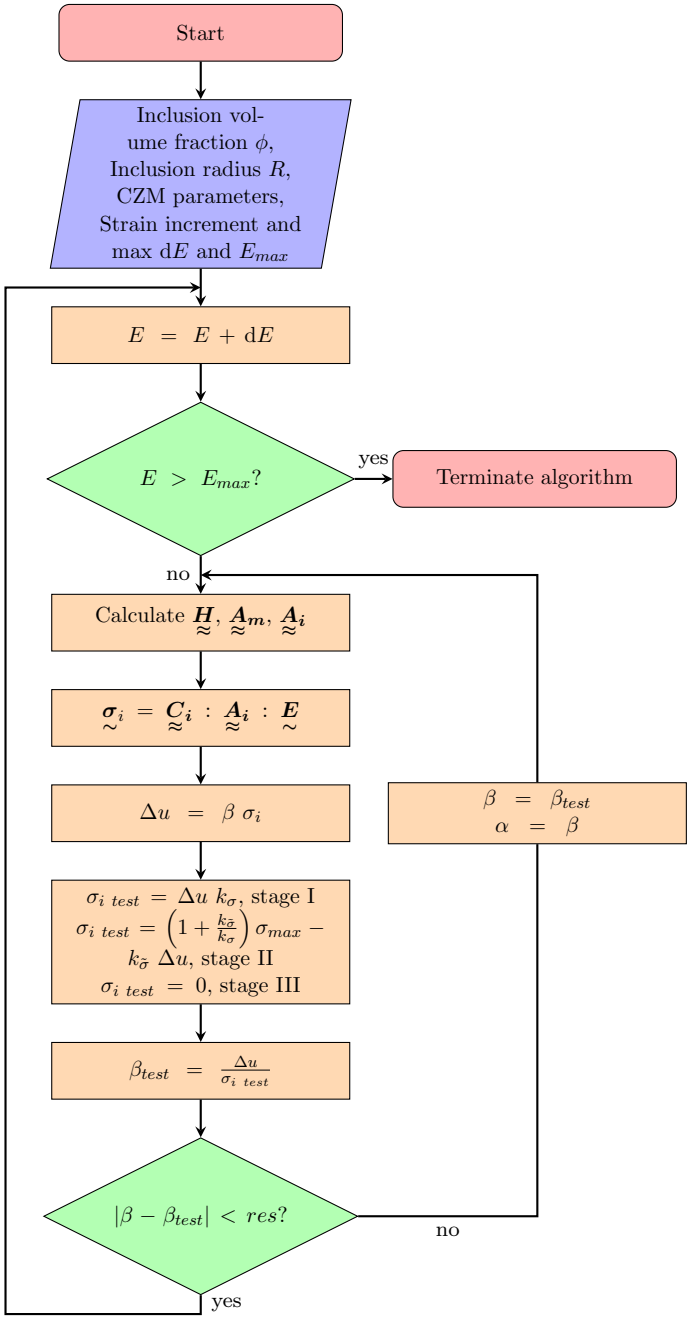

Figure 4: Flowchart of the proposed homogenisation model

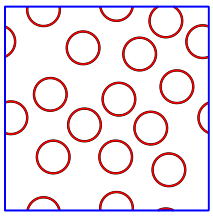

Figure 5: RVE obtained with the Dropping and Rolling algorithm ($\phi = 30\%$, $R = 80$ μm).

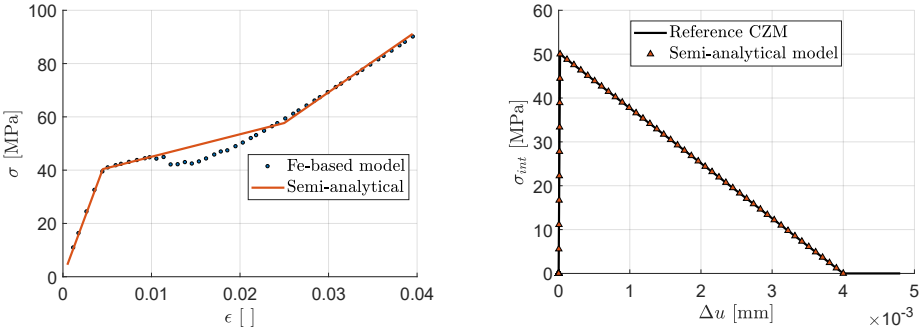

(a) (b)

Figure 6: (a) Homogenised stress-strain curves from the numerical and semi-analytical models under bi-axial loading;
(b) Associated stress-displacement curve obtained at the interface of the inclusion.

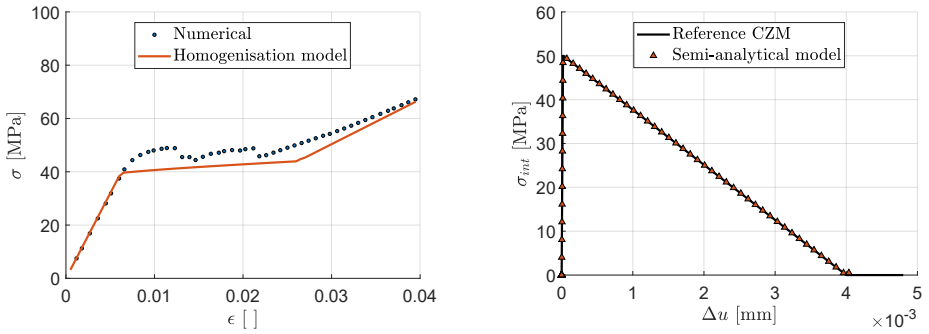

(a) (b)

Figure 7: (a) Homogenised stress-strain curves from the numerical and semi-analytical models under uniaxial loading;
(b) Associated stress-displacement curve obtained at the interface of the inclusion.

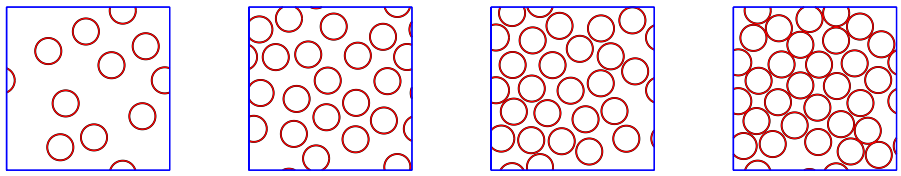

$\phi = 20\%$ $\phi = 40\%$ $\phi = 50\%$ $\phi = 60\%$

Figure 8: Microstructures obtained from the Dropping and Rolling algorithm [22].

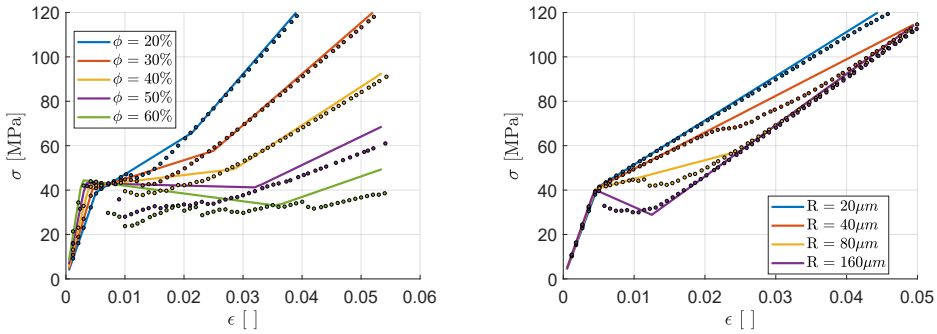

(a) (b)

Figure 9: Homogenisedtress-strain curves from the numerical (dotted lines) and semi-analytical models under bi-axial loading, (a) effect of inclusion volume fraction, (b) effect of inclusion size.

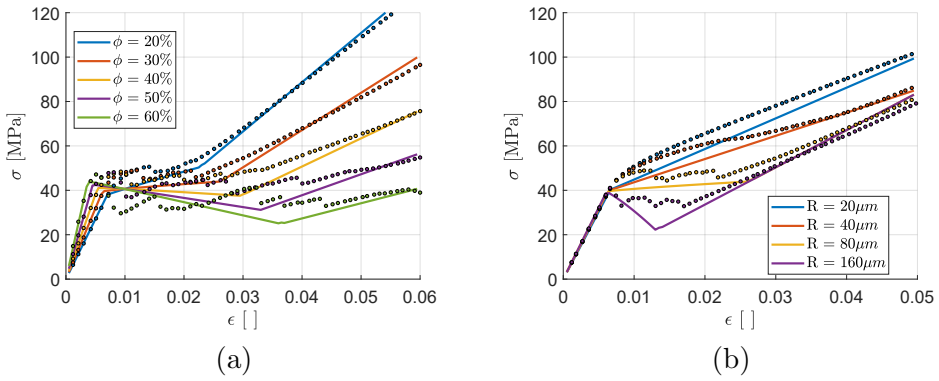

Figure 10: Homogenisedtress-strain curves from the numerical (dotted lines) and semi-analytical models under bi-axial loading, (a) effect of inclusion volume fraction, (b) effect of inclusion size.